AIAA JOURNAL
Vol. 44, No. 3, March 2006

Shell Buckling Design Criteria Based on Manufacturing Imperfection Signatures

Mark W. Hilburger,* Michael P. Nemeth,† and James H. Starnes Jr.‡
NASA Langley Research Center, Hampton, Virginia 23681-0001

An analysis-based approach for developing shell-buckling design criteria for laminated-composite cylindrical shells that accurately account for the effects of initial geometric imperfections is presented. With this approach, measured initial geometric imperfection data from six graphite–epoxy shells are used to determine a manufacturing-process-specific imperfection signature for these shells. This imperfection signature is then used as input into nonlinear finite element analyses. The imperfection signature represents a first-approximation mean imperfection shape that is suitable for developing preliminary-design data. Comparisons of test data and analytical results obtained by using several different imperfection shapes are presented for selected shells. These shapes include the actual measured imperfection shape of the test specimens, a first-approximation mean imperfection shape, with and without plus or minus one standard deviation, and the linear-bifurcation-mode imperfection shape. In addition, buckling interaction curves for composite shells subjected to combined axial compression and torsion loading are presented that were obtained by using the various imperfection shapes in the analyses. A discussion of the nonlinear finite element analyses is also presented. Overall, the results indicate that the analysis-based approach presented for developing reliable preliminary-design criteria has the potential to provide improved, less conservative buckling-load estimates and to reduce the weight and cost of developing buckling-resistant shell structures.

Nomenclature

A_{kl}, B_{kl}	=	Fourier coefficients
k, l	=	axial half-wave number, circumferential full-wave number
L	=	total cylinder length
L_t	=	cylinder test length
P	=	applied axial compression load
P_{bif}	=	predicted linear bifuraction buckling loads for axial compression
R	=	cylinder radius
T	=	applied torsion load
T^{+}_{bif}	=	predicted linear bifuraction buckling loads for torsion
t, t_0, t_{nom}	=	cylinder thickness, measured thickness, nominal thickness
V	=	coefficient of variation
w_0, $\bar{w}_0$	=	measured midsurface imperfection, normalized midsurface imperfection
x, θ	=	axial and circumferential coordinates
μ_0, $\bar{\mu}_0$	=	mean imperfection shape, normalized mean imperfection shape
σ_0, $\bar{\sigma}_0$	=	imperfection standard deviation, normalized imperfection standard deviation

Presented as Paper 2003-1843 at the AIAA/ASME/ASCE/AHS/ASC 44th Structures, Structural Dynamics, and Materials Conference, Norfolk, VA, 7–10 April 2003; received 24 September 2003; revision received 16 February 2005; accepted for publication 20 February 2005.

This paper is dedicated to our good friend and mentor Dr. James H. Starnes Jr. His vision of improved design technologies for composite structures played a major role in guiding much of the research conducted at LaRC over the years, including the research presented in this paper.

*Aerospace Engineer, Mechanics of Structures and Materials Branch. Member AIAA.

†Senior Research Engineer, Mechanics of Structures and Materials Branch. Associate Fellow AIAA.

‡Senior Engineer, Structures and Materials Competency; deceased 27 October 2003. Fellow AIAA.

Introduction

HIGH-PERFORMANCE aerospace shell structures are inherently thin walled because of weight and performance considerations and are often subjected to destabilizing loads. In addition, fiber-reinforced composite materials are becoming more common in aerospace vehicle structures because of their high strength, high stiffness, and amenability to structural tailoring that permits design solutions that are not possible with metals. Thus, buckling is an important and often critical consideration in the design of these structures, and reliable, validated design criteria for thin-walled shells are needed, especially for shells made of advanced composite materials.

As one might expect, shell-buckling design criteria have a history steeped in empiricism.[1,2] From approximately 1930 to 1967, many shell-buckling experiments were conducted on metallic shells. Typically, the experiments yielded buckling loads that were substantially lower than the corresponding analytical predictions, which were based on simplified linear bifurcation analyses of geometrically perfect shells with nominal dimensions and idealized support conditions. The seminal works by von Kármán and Tsien,[3] Donnell and Wan,[4] and Koiter[5] identified small deviations from the idealized geometry of a shell, known as initial geometric imperfections, as a primary source of discrepancy between corresponding analytical predictions and experimental results. However, it appears that, because of the intense computational requirements of the nonlinear analyses used by von Kármán and Tsien and by Donnell and Wan, and the asymptotic analyses used by Koiter, at that time, buckling design allowables were determined by establishing lower bounds to test data. Specifically, empirical factors that have become known as knockdown factors were determined and were to be used in conjunction with linear bifurcation analyses for simply supported shells that is, these empirical factors were used to knockdown the unconservative analytical prediction. This approach to shell buckling design remains prominent in industry practice, as evidenced by the extensive use of the NASA space vehicle design criteria.[6–8]

From approximately 1960 to 1989, digital computers emerged and matured as a practical tool for scientists and engineers. With these computational tools, considerable effort was put forth to determine analytically the effects of initial geometric imperfections on the buckling response of shells. These efforts were largely based on Koiter's asymptotic theory[5] (see Refs. 1 and 9) for idealized structural shapes with nominal dimensions and also included investigations of shells made of fiber-reinforced composite materials.[10–13]

In addition, in-depth, substantial experimental investigations that focused on fiber-reinforced composite shells were conducted at institutions such as NASA Langley Research Center and Wright Aeronautical Laboratories at Wright–Patterson Air Force Base, in addition to various academic institutions worldwide. It was during this time period that the measurement of initial geometric imperfections in test specimens and high-fidelity response measurement techniques and apparatus were recognized as important elements in the development of design criteria for buckling of shells.[14–17]

Another significant development that occurred in parallel with the maturation of digital computers in the 1960s to 1980s was the development of computational structural analysis codes based on finite difference or finite element methods. Two prominent examples that stimulated the development of this particular technology are the NASA Structural Analysis code (NASTRAN[18]) and the Structural Analysis of General Shells code (STAGS[19]), which were funded by the U.S. Government. The successors and inheritors of these codes now possess robust static and dynamic nonlinear analysis capabilities, along with extensive graphics capabilities, that enable scientists and engineers to model and visualize experiments or actual flight hardware to an enormous level of detail. Archetypal examples of the application of these tools are the in-depth, highly detailed studies of cylinder buckling response documented in Refs. 20–22 and the comprehensive and highly detailed nonlinear and buckling analyses of the space shuttle superlightweight external fuel tank that is documented in Refs. 23–27. In addition, the extension of these analysis techniques and codes to other disciplines has helped to enable the development of advanced experimental-response measurement systems. Thus, the tools and understanding now exist for developing high-fidelity shell buckling design criteria for shells of general shape and material composition and for combined mechanical and thermal loads.

Recent advances and recommendations for the development of modern shell-buckling design criteria have been given in Refs. 28 and 29. These references examine the potential benefits of adopting probabilistic and hybrid probabilistic-deterministic approaches for developing design criteria. An important concept that is discussed in Ref. 29 and used in the present study is the establishment of characteristic imperfection signatures that are associated with the different shell-manufacturing processes. This concept is based on the idea that each manufacturing process will yield shells that possess essentially similar initial geometric imperfection shapes, with a well-defined range of pointwise amplitudes. With this information established, high-fidelity analyses and selective structural testing can be used to determine refined, reliable design criteria for shell buckling that are not overly conservative like the present lower-bound approach found in NASA SP 8007.[6] To this end, some effort has been put toward defining initial geometric imperfection models to be used in shell analysis for isotropic and composite shells.[30,31] Similarly, various probability-based analysis methods have been proposed to develop reliable design buckling loads for imperfect shells in which approximations to the measured imperfections are used in the analyses.[32,33]

The present study focuses on the development of a refined shell-buckling preliminary-design criteria that is based on high-fidelity nonlinear finite element analyses that include the effects of a manufacturing-process-specific geometric imperfection signature. Refined preliminary-design data are important because they substantially reduce the chance of getting locked-in to a poor design early in a vehicle-development program and, in the context of stability-critical thin-walled shell structures, can give a more accurate preliminary prediction of the load-carrying capacity of the shell. One main objective of the present study is to establish a first-approximation characteristic imperfection signature for selected circular cylindrical shells made of a graphite–epoxy material that can be used to develop data suitable for preliminary design. Another main objective is to develop and validate an analysis-based shell-buckling design criteria that accurately accounts for the effects of initial geometric imperfections by using the imperfection signature defined herein. The final objective is to illustrate the potential improvements in buckling predictions that can be realized, particularly for combined loading conditions. Toward these objectives, the testing and analysis procedures that are used in the present study are discussed first. Next, the details of how measured geometric imperfections for six laminated graphite–epoxy shells are used to determine a manufacturing imperfection signature are presented. Then, analysis results and experimental results for selected compression-loaded shells are compared to validate the new analysis-based procedure for developing design criteria. Finally, numerically predicted buckling-interaction curves are presented for three different shells subjected to combined axial compression and torsion to illustrate the potential benefits of the new procedure.

Test Specimens, Imperfection Measurements, and Tests

Six test specimens used in the present study are described in this section. These specimens were previously fabricated and tested at the NASA Langley Research Center in support of a research program to study the effects of initial imperfections on the nonlinear response and buckling of compression-loaded composite shells. Much of this work has been documented in Refs. 20–22, and selected details about the test specimens, imperfection measurements, and tests are summarized in this section. Additional details on the cylinder tests may be found in Refs. 20–22.

Test Specimens

The specimens were fabricated from 12-in. (304.8-mm)-wide, 0.005-in. (0.127-mm)-thick AS4/3502 unidirectional graphite–epoxy tape material. The nominal unidirectional lamina properties of a typical 0.005-in.-thick ply with a fiber volume fraction of 0.62 are as follows: longitudinal modulus $E_1 = 18.5$ Msi (127.5 GPa), transverse modulus $E_2 = 1.64$ Msi (11.3 GPa), in-plane shear modulus $G_{12} = 0.87$ Msi (5.99 GPa), and major Poisson's ratio $\nu_{12} = 0.30$. The material was laid up by hand on a 15.75-in. (400.05-mm)-diam mandrel and vacuum bagged and cured in an autoclave to form six shells with different shell-wall laminates. These shells include shells with an 8-ply axially stiff $[\mp 45/0_2]_s$ laminate, an 8-ply circumferentially stiff $[\mp 45/90_2]_s$ laminate, an 8-ply quasi-isotropic $[\mp 45/0/90]_s$ laminate, a 16-ply axially stiff $[\mp 45/0_2]_{2s}$ laminate, a 16-ply circumferentially stiff $[\mp 45/90_2]_{2s}$ laminate, and a 16-ply quasi-isotropic $[\mp 45/0/90]_{2s}$ laminate. These six shells are referred to herein as shells or specimens C1–C6, respectively. These specimens had a nominal length of 16.0 in. (406.4 mm) and a nominal radius of 8.0 in. (203.2 mm). The 8-ply and 16-ply specimens had a nominal shell-wall thickness of 0.040 in. (1.016 mm) and 0.080 in. (2.032 mm), respectively, and had shell-radius-to-thickness ratios of 200 and 100, respectively. Both ends of the specimens were potted in an aluminum-filled epoxy resin to ensure that the ends of the specimen did not fail prematurely during the test. The potting material extended approximately 1.0 in. (25.4 mm) along the length of the specimens at each end, resulting in a test section that is approximately 14.0 in. (355.6 mm) long. The ends of the specimens were machined flat and parallel to facilitate proper load introduction during the tests. A photograph of a typical test specimen and the specimen coordinate system used to represent the corresponding geometry is shown in Fig. 1. The nominal cylinder length, test-section length, radius, and thickness are designated as L, L_t, R, and t, respectively.

Imperfection Measurements

Three-dimensional surveys of the inner shell-wall surface of the specimens were made before testing determine the initial geometric shell-wall imperfection shape. Measurements were taken over a uniform grid with increments of 0.125 in. (3.175 mm) in the axial direction and 0.139 in. (approximately 1 deg of arc) in the circumferential direction over the exposed surfaces of the specimens. A typical contour plot of the normalized initial geometric shell-wall midsurface imperfections $\bar{w}_0(x, \theta)$ for specimen C3 is shown in Fig. 2. The measured shell-wall imperfection w_0 is normalized by the nominal shell-wall thickness $t_{\text{nom}} = 0.040$ in. (1.016 mm). These results indicate that the initial geometric shell-wall imperfection is periodic in the circumferential direction and exhibits slight variations in the axial direction. The amplitude of the imperfection varies from $+1.27t_{\text{nom}}$ to $-1.536t_{\text{nom}}$.

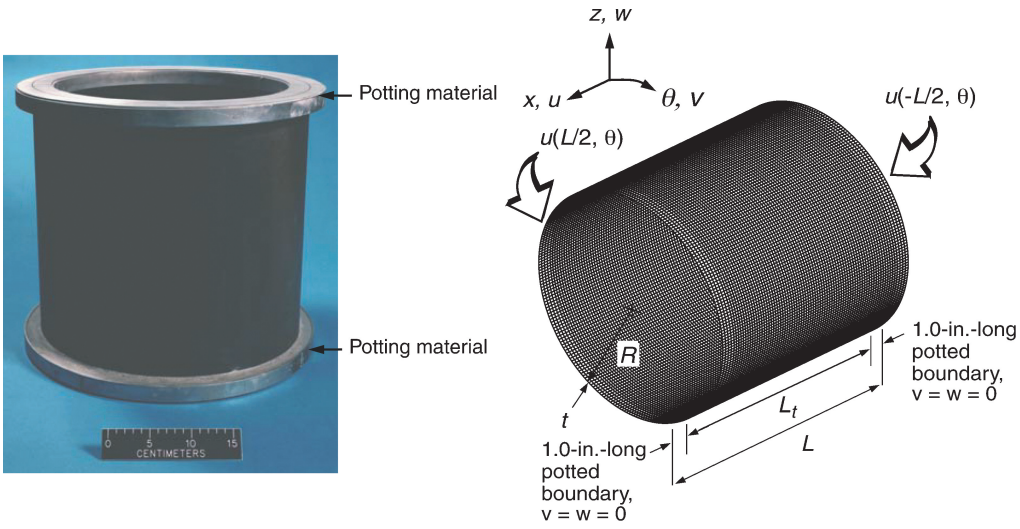

Fig. 1 Typical specimen and finite element model geometry and boundary conditions.

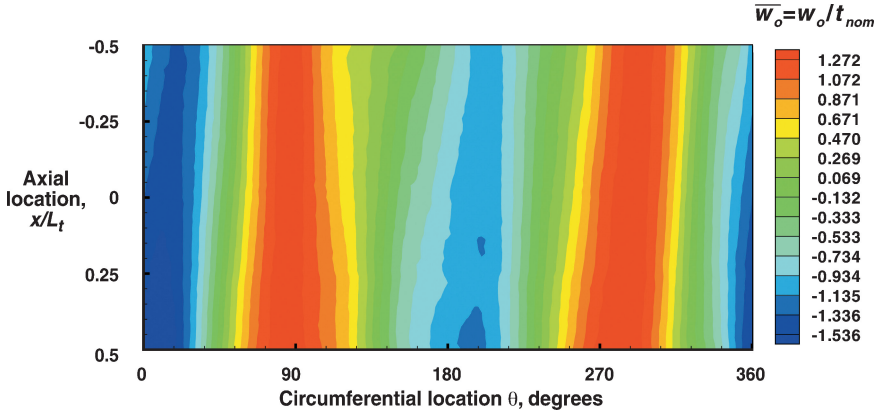

Fig. 2 Typical measured inner-surface imperfection shape for shell C3.

Test Apparatus and Tests

The specimens were instrumented with electrical-resistance strain gauges, and direct-current differential transducers (DCDTs) were used to measure displacements. Three noncollinear DCDTs were positioned in three corners of the upper loading platen and used to measure the end-shortening displacement and the platen rotations. A shadow moiré interferometry technique was used to observe the shell-wall prebuckling, buckling, and postbuckling radial deformation patterns. All data were recorded with a data acquisition system, and the moiré patterns were recorded photographically, on videotape, and with a high-speed digital video camera.

The specimens were loaded in compression with a 120-Kip (534-kN) hydraulic universal-testing machine by applying an end-shortening displacement to the shell ends. To control the load introduction into the specimen, the upper loading platen was aligned with the loading surface of the specimen before the test by adjusting leveling bolts in the corners of the upper loading platen until strains measured by selected strain gauges on the specimens indicated a uniform axial strain distribution in the shell wall. The specimens were loaded until global collapse of the shells occurred.

Finite Element Models and Analyses

The finite element models and analysis methods used in the present study are based on experimentally validated models presented Refs. 21 and 22. In particular, the results presented in Refs. 21 and 22 indicate that highly accurate buckling responses can be predicted for compression-loaded shells if initial geometric imperfections, material property variability, nonuniform thickness distribution, and other features are modeled to a high degree of accuracy. Such validated models that include the effects of these details are referred to as high-fidelity models and are generally deemed necessary to develop the most accurate, analysis-based, high-fidelity design criteria. In line with the objectives of the current study, only the effects of the initial geometric imperfection are included in the numerical models. However, the model details, such as the mesh refinement and idealized boundary conditions, and the analysis methods are the same as those used in the previous studies, and as a result, the solutions are expected to be converged. In addition, the validated finite element models used for compression-loaded shells are also used for the analysis of the torsion-loaded shells and the shells subjected to combined torsion and compression presented herein and are expected to be converged because of the finite element models extensive refinement. Additional details on the finite element models and analysis procedures are found in Refs. 21 and 22.

Finite Element Models

The shells considered in this study were analyzed with the STAGS nonlinear shell-analysis code.[19] STAGS is a finite element code developed for the static and dynamic analysis of general shells and includes the effects of geometric and material nonlinearities in the analysis. A typical finite element model of a specimen is shown in Fig. 1. The standard 410 quadrilateral element from the STAGS element library was used in the models, which is a flat facet-type element that is based on the Kirchhoff–Love shell hypothesis and the nonlinear Lagrangian strain tensor. The element nodes include three translational degrees of freedom and three rotational degrees of freedom. Large element rotations are accounted for by using a corotational algorithm. Typically, the elements of the finite element mesh are approximately 0.2×0.2 in. (0.5×0.5 mm) square. However, some of the elements near the boundary region of the shell are

somewhat smaller to represent accurately the bending boundary-layer response near the end of the shell. Each element possesses four integration points, which are distributed in such a way as to provide a modeling resolution of approximately 0.1×0.1 in. (0.25×0.25 mm) square. This integration-point spacing is on the order of the measurement-point spacing used when measuring the initial geometric imperfections of the specimens.

Compression-loaded shells and shells subjected to combined axial compression and torsion are analyzed in the present investigation. To simulate the constraints provided by the potting material in a compression-loaded shell, the circumferential and radial displacements v and $w$were set equal to zero in edge regions of the shell as indicated in Fig. 1. Similarly, for shells subjected to combined axial compression and torsion, the radial displacement w was set equal to zero and the circumferential displacement v was applied to simulate a torsion load.

Nonlinear Analysis Procedure

The prebuckling, buckling, and postbuckling responses of the shells were determined by using the following analysis procedure. The prebuckling responses were determined by using the Riks pseudoarc-length path-following method[34] in STAGS until just before buckling occurred. The unstable buckling response of a shell was predicted by using the nonlinear, transient-analysis option of the code. The transient-analysis option in STAGS uses proportional structural damping and an implicit numerical time-integration method developed by Park.[35] The transient analysis was initiated from an unstable equilibrium state close to the limit point by incrementing the end displacement by a small amount. An initial time step of 1.0^{-8} s was used in the analysis, and the time step was automatically adjusted by the program as a function of the solution behavior. The transient analysis was continued until the kinetic energy in the shell had dissipated to a negligible level, which indicated that the transient response had attenuated. Once the transient analysis had attenuated to a near-steady-state solution, the load-relaxation option of the code was used to establish the stable static equilibrium state. Results from conventional linear bifurcation buckling analyses were also determined with STAGS for comparison with the nonlinear response results.

Manufacturing Imperfection Signature

Shell-wall geometric imperfections that had been measured previously[20–22] for the six laminated-composite shells considered herein were used to identify a manufacturing-process-specific first approximation imperfection signature for this type of structure. First, a reference or best-fit cylinder for the initial imperfection measurement data for each shell was determined. Specifically, a data reduction program that uses the method of least squares was used to compute the rigid-body translations and rotations and the mean radius of each cylinder. Then, the measured radial imperfections, deviations from a perfect cylinder, were recalculated with respect to the corresponding new best-fit cylinder. The measured imperfection data was then represented by a two-dimensional half-wave Fourier cosine series given by

$$w_0(x,\theta) = t_{\text{nom}} \sum_{k=0}^{N} \sum_{l=0}^{N} \cos\left(\frac{k\pi x}{L}\right)\left[A_{kl} \cos\left(\frac{l\pi x}{L}\right) + B_{kl} \sin(l\pi\theta)\right] \tag{1}$$

where R, L, and t_{nom} are the shell radius, length, and wall thickness; x and θ are the axial and circumferential coordinates; and k and l are integers denoting the number of axial half-waves and circumferential full-waves, respectively. Using a standard representation of this type for the measured imperfection enables convenient analysis and comparison of different imperfection distributions from different shells and different manufacturing processes. For example, the coefficient distribution of a half-wave Fourier cosine representation of the measured geometric imperfection shape for shell specimen C3 is presented in Fig. 3. The results indicate that the largest-magnitude component of the imperfection is the $k = 0$ and $l = 2$ component and that the magnitudes of the other components decrease rapidly as the wave numbers k and l increase. The $k = 0$ and $l = 2$ component corresponds to a cylinder with an elliptical cross section that has a magnitude of $1.2t_{\text{nom}}$. The next largest component is associated with $k = 1$ and $l = 2$ and has a magnitude of approximately $0.2t_{\text{nom}}$. In general, the dominant coefficients are associated with the long wavelength imperfections in the circumferential and axial directions. Coefficients for values of k and $l > 10$ have a negligible effect on the overall imperfection shape. However, the short wavelength components are retained in the imperfection model because these modes may be associated with high imperfection sensitivity for the shells considered herein even though their magnitudes are generally very small.[36] Results for shells C1, C2, and C4–C6 indicate similar coefficient distributions and suggest that a manufacturing-process-specific imperfection signature for graphite–epoxy laminated-composite shells can be established in terms of a characteristic Fourier coefficient distribution and range. To this end, a mean imperfection shape and a corresponding standard deviation to the imperfection shape were determined based on the measured imperfection data. The mathematical expectation or mean value of $w_0(x,\theta)$ is given by

$$\mu_w(x,\theta) = \langle w_0(x,\theta)\rangle = t_{\text{nom}} \sum_{k=0}^{N} \sum_{l=0}^{N} \cos\left(\frac{k\pi x}{L}\right) \times \left[\langle A_{kl}\rangle \cos\left(\frac{l\pi x}{L}\right) + \langle B_{kl}\rangle \sin(l\pi\theta)\right] \tag{2}$$

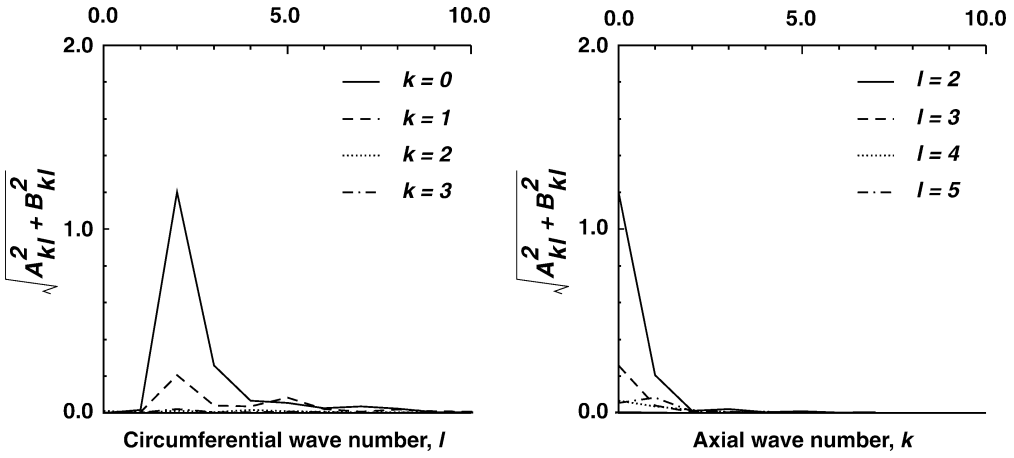

Fig. 3 Coefficient distribution of Fourier series representation of measured imperfection shape for shell C3.

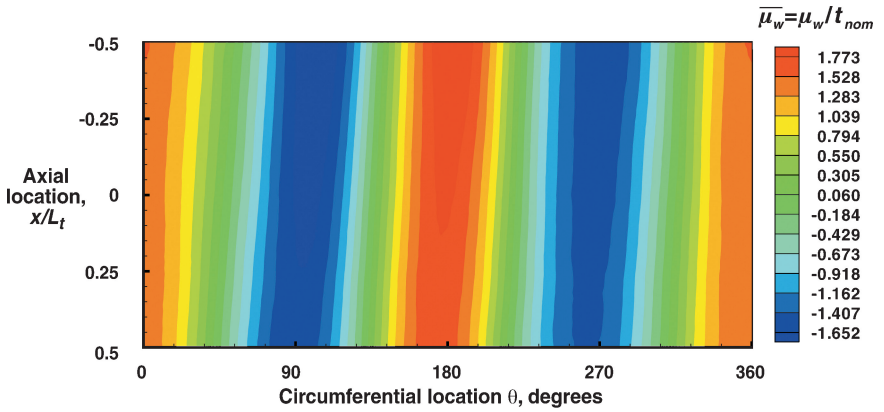

Fig. 4 Calculated first-approximation mean imperfection signature.

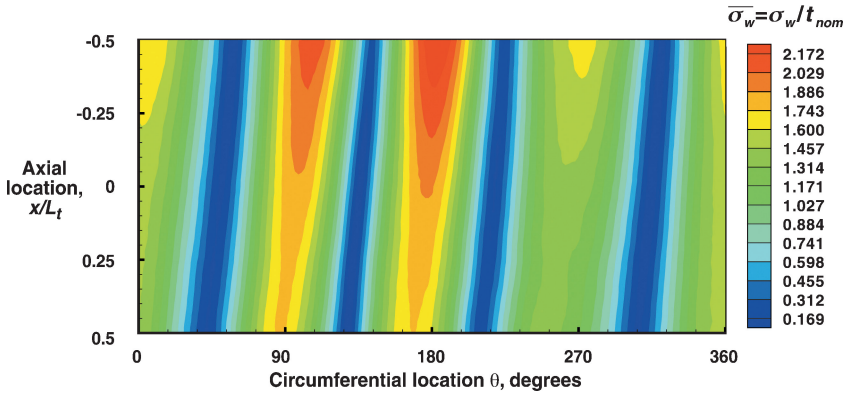

Fig. 5 Calculated standard deviation to imperfection signature shown in Fig. 4.

where $\langle\,\rangle$ denotes the mean value. A contour plot of the normalized mean geometric imperfections $\mu_w(x,\theta)$ is shown in Fig. 4. The mean shell-wall imperfection μ_w is normalized by the nominal shell-wall thickness $t_{\text{nom}} = 0.04$ in. These results indicate that the initial geometric shell-wall imperfection is periodic in the circumferential direction, exhibits slight variations in the axial direction, and is similar in character to the measured imperfection shape for shell C3 shown in Fig. 2. The amplitude of the imperfection μ_w varies from $+1.77t_{\text{nom}}$ to $-1.65t_{\text{nom}}$. The corresponding standard deviation of the geometric imperfection shape $\sigma_w(x,\theta)$ is defined by

$$\sigma_w^2[w_0(x,\theta)] = \left\langle [w_0(x,\theta) - \langle w_0(x,\theta)\rangle]^2 \right\rangle \tag{3}$$

A contour plot of the corresponding normalized standard deviation of the geometric imperfection shape is shown in Fig. 5. The results indicate that the maximum standard deviation is equal to $2.172t_{\text{nom}}$ and is primarily associated with long wavelength components of the imperfection shape. In addition, the coefficient of variation was calculated for each component of the imperfection and gives the relationship between the mean and the standard deviation. The coefficient of variation, denoted by V, is given by

$$V = \sigma(X_{kl})/\mu(X_{kl}) \tag{4}$$

where

$$X_{kl} = \sqrt{A_{kl}^2 + B_{kl}^2} \tag{5}$$

A typical plot of V for an axial half-wave number $k = 0$ is shown in Fig. 6. The results indicate that V is relatively high for long wavelength imperfections, for example, $V = 1.6$ for $k = 0$ and $l = 2$, and decreases rapidly to a value of approximately 0.5 for $l < 20$. Results for the other values of k were also obtained and indicate similar trends. This information suggests that an approximate expression

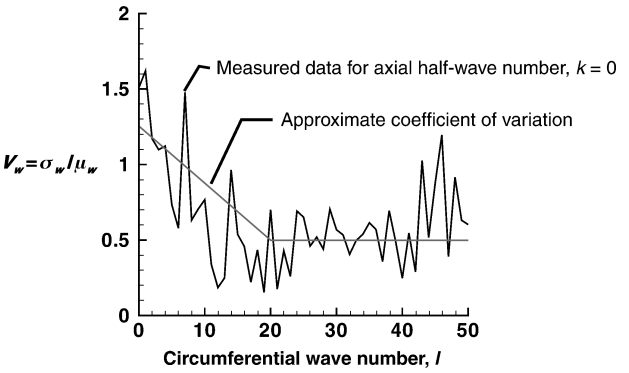

Fig. 6 Coefficient of variation for axial half-wave number $k = 0$ as function of circumferential wave number l.

that relates the mean coefficient values with the corresponding standard deviation can be developed. For example, an approximate V relationship for this particular case that is applicable for all values of k is given by

$$V = \begin{cases} 1.25 - (0.75/20)l, & 0 \le l \le 20 \\ 0.5, & 20 \le l \le 50 \end{cases} \tag{6}$$

This equation is used in subsequent sections when defining simulated imperfections in place of the exact standard deviation function given in Eq. (3) to simplify the calculations.

Response of Compression-Loaded Shells

The effects of five different imperfection shapes on the response of the three compression-loaded 8-ply shells C1–C3 were investigated

Table 1 Numerically predicted and experimentally measured buckling loads for compression-loaded shells

Shell	Predicted buckling loads, lbf (kN)						
	Perfect shell	Measured imperfection	Mean imperfection, μ	$\mu+\sigma$ Imperfection	$\mu-\sigma$ Imperfection	Linear-bifurcation-mode imperfection $w_0/t_{\text{nom}}=0.5$	Experimental buckling load
C1	29,900	29,300	29,000	27,500	29,850	17,040	27,788
	(133.0)	(130.0)	(129.0)	(122.3)	(132.8)	(75.8)	(123.6)
C2	36,300	34,400	36,170	34,430	36,930	14,470	31,924
	(161.5)	(153.0)	(160.9)	(153.1)	(164.3)	(64.4)	(142.0)
C3	41,500	38,180	39,100	36,400	40,200	21,300	34,082
	(184.6)	(169.8)	(173.9)	(161.9)	(178.8)	(94.7)	(151.6)

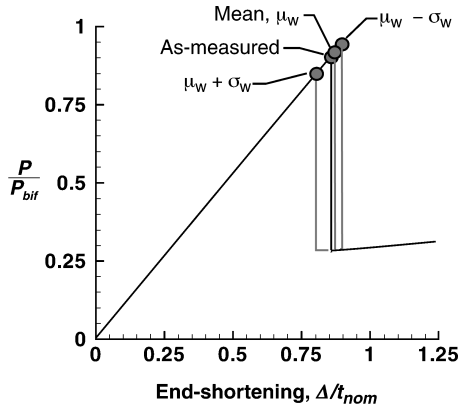

a) Predicted load–end-shortening response, selected imperfections

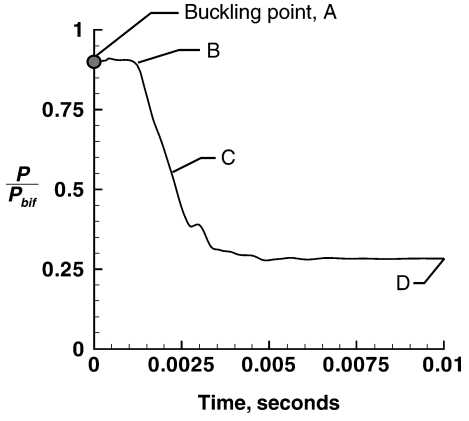

b) Predicted load-time history during collapse, actual measured imperfection

Fig. 7 Predicted nonlinear response for compression-loaded quasi-isotropic shell C3 with various imperfection shapes.

in the current study. Specifically, the effects of actual measured shell-wall imperfections, simulated imperfections that are based on the first approximation imperfection signature, and linear-bifurcation-mode imperfections were analyzed. The simulated first approximation imperfection signature includes the mean imperfection with and without plus or minus one standard deviation. Load-shortening response curves and shell deformations are presented subsequently for the quasi-isotropic shell C3 that illustrate the overall response characteristics for the compression-loaded shell with the five different imperfection shapes. In addition, predicted buckling loads for the two orthotropic 8-ply shells C1 and C2 with the five different imperfection shapes are also presented. Moreover, the predicted buckling loads are compared to the actual experimental buckling loads and to the design load one would get by extrapolating the results in NASA SP-8007 for isotropic shells to the composite shells.

Four predicted load-shortening response curves are presented for shell C3 in Fig. 7a and include results for a shell with the actual measured imperfection shape; a shell with the mean imperfection shape, denoted by μ_w; a shell with the mean imperfection shape plus one standard deviation, denoted by $\mu_w+\sigma_w$; and a shell with the mean imperfection shape minus one standard deviation, denoted by $\mu_w-\sigma_w$. The axial load P and end shortening Δ are normalized with respect to the linear bifurcation buckling load of the geometrically perfect nominal shell, $P_{\text{bif}}=42{,}590$ lbf (189.4 kN), and the nominal shell-wall thickness, $t_{\text{nom}}=0.040$ in. (1.016 mm), respectively. The load–end-shortening curves clearly indicate a linear prebuckling response. The general instability occurs in the shell at normalized axial load levels that range from $P/P_{\text{bif}}=0.855$, for a shell with $\mu_w+\sigma_w$ imperfection shape, to 0.943 for the shell with a $\mu_w-\sigma_w$ imperfection shape. The predicted buckling loads are summarized in Table 1. The general-instability response of the shell is followed by a sudden reduction in the axial load supported by the shell that is associated with the transient collapse response of the shell. The results indicate that the postbuckling load level is insensitive to the different types of imperfections considered herein. The corresponding load-time history of the transient collapse response of shell C3 with the actual measured imperfections is shown in Fig. 7b. The load-time history curve exhibits a sudden reduction in axial load until the collapse response attenuates and the axial load achieves a steady-state value. The kinetic energy in the shell obtains a maximum value during the transient collapse response and dissipates over time, and the shell reaches a stable postbuckling equilibrium state after approximately 0.007–0.008 s. The shell exhibits postbuckling load-carrying capacity, however, the effective axial stiffness of the specimen is significantly reduced in the postbuckling range of loading, as indicated by the large reduction in the slope of the load-shortening response curves. This reduction in effective axial stiffness is caused by large-magnitude radial deformations that develop in the specimen during buckling, which result in significant load redistribution in the specimen and reduce the effective, load-carrying cross section of the cylinder.

The transient deformation responses for selected time steps during the transient collapse response of shell C3 with the actual measured imperfection, indicated by the letters A–D in Fig. 7b, are presented in Figs. 8a–8d, respectively. Just before buckling occurs, the shell wall deformations are characterized by several localized ellipselike buckles, as indicated in Fig. 8a. The localization in the deformation pattern is caused by the combination of a local geometric shell-wall imperfection that is in the form of a significant variation in the shell-wall geometry and the bending boundary-layer deformations that form near the end of the shell. In addition, the localized deformations occur in regions with destabilizing compressive axial and circumferential stresses. The coupling of these destabilizing stresses and the local deformations cause the buckling response in the shell. After approximately 0.0012 s have elapsed in the transient response, a single ellipselike buckle has grown in amplitude and couples with the destabilizing stresses in the shell wall to cause the general instability and collapse of the shell. The magnitude of the shell-wall radial displacement varies $\pm 0.5t_{\text{nom}}$. After additional time has elapsed in the transient collapse response, additional local buckles have formed around the circumference and along the length of the shell, as indicated in Fig. 8c, and the normalized axial load has decreased from 0.890 to 0.554. In addition, some of the buckles in the shell begin to coalesce into larger diamond-shaped buckles.

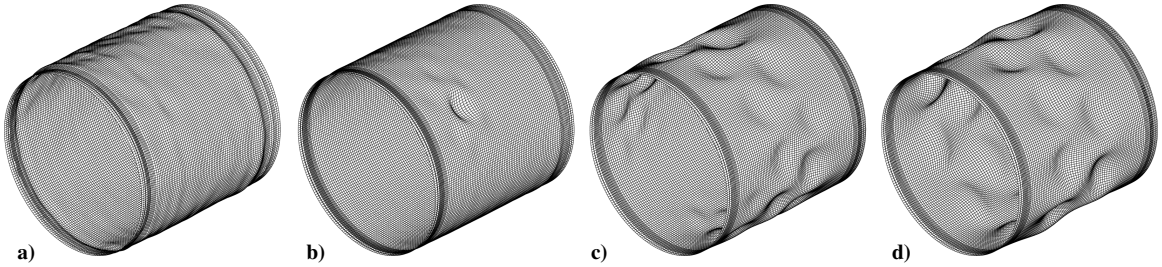

Fig. 8 Predicted buckling deformation response for shell C3 with actual measured initial imperfection.

a) Mean imperfection μ_w, time = 0.0011 s, $P/P_{cr} = 0.918$ **b) $\mu_w + \sigma_w$ imperfection, time = 0.0012 s, $P/P_{cr} = 0.855$** **c) $\mu_w - \sigma_w$ imperfection, time = 0.0010 s, $P/P_{cr} = 0.943$**

Fig. 9 Typical initial buckling deformation responses for shell C3 with selected simulated initial imperfections.

The magnitude of the shell-wall radial displacement varies between $+3t_{nom}$ and $-7t_{nom}$. After approximately 0.01 s have elapsed in the transient response, the kinetic energy in the shell has dissipated to a negligible level, indicating that the transient response has attenuated and the shell has deformed into a stable postbuckling mode-shape, as indicated in Fig. 8d. As loading continues in postbuckling region, the diamond-shaped buckles increase in size and the magnitude of the radial deformations of the buckles and the outer-surface ridges increase to between $+4t_{nom}$ and $-9t_{nom}$.

Deformation results were obtained for shell C3 with the mean imperfection shape, the $\mu_w + \sigma_w$ imperfection shape, and $\mu_w - \sigma_w$ imperfection shape and indicated similar response characteristics to those exhibited by the shell with the actual measured imperfection. In particular, predicted initial buckling deformations for shell C3 are presented in Figs. 9a–9c. These results indicate that the initial buckling deformation response of a shell with the mean imperfection μ_w and the $\mu_w + \sigma_w$ imperfection are similar to that exhibited by the shell with the actual measured imperfection and are characterized by a localization of a single buckle near one end of the shell. In contrast, the shell with the $\mu_w - \sigma_w$ imperfection shape exhibits distributed initial buckling deformations shown in Fig. 9c that are similar to those exhibited by the corresponding geometrically perfect shell. These results are significant because they suggest that the use of a mean imperfection shape and the corresponding standard deviation can bound the experimental buckling loads as well as predict physically meaningful response characteristics such as the buckling deformations. Results were also obtained for the two 8-ply orthotropic shells C1 and C2. In particular, buckling loads for the various imperfection shapes were calculated and are also presented in Table 1. Most notable is the fact that the predicted buckling loads for the shells with the actual measured imperfection are bounded by the results for the shells with the $\mu_w + \sigma_w$ imperfection shape and $\mu_w - \sigma_w$ imperfection shape. In addition, the experimental results agree well with the predicted results that include the effects of the actual measured geometric imperfection. The correlation would improve still further if other measured imperfections were included in the finite element model, for example, measured thickness variation, material property variation, and loading nonuniformities, as shown in Refs. 21 and 22. Specifically, the measured thickness imperfection has been shown to account for an additional 5–10% reduction in the buckling load of the shells. In contrast, the results for shells with linear-bifurcation-mode imperfections are, for an imperfection amplitude equal to 0.5 times the nominal wall thickness, ultraconservative. Similarly, the lower-bound design recommendation given in NASA SP-8007 for the corresponding isotropic shell is equal to $P/P_{bif} = 0.47$, which is also ultraconservative, as expected.

Table 2 Numerically predicted linear bifurcation buckling loads (stress resultants) for geometrically perfect 8-ply shells

Shell	P_{bif}, lbf (kN)	T_{bif}, lbf · ft (N · m)
C1	29,780 (132.5)	6800.9 (9220.2)
C2	36,660 (163.1)	6180.5 (8379.2)
C3	42,580 (189.4)	6416.0 (8698.5)

Response of Shells Subjected to Combined Axial Compression and Torsion

A numerical study of the effects of the four different imperfection shapes on the buckling load of the 8-ply shells C1–C3 subjected to combined axial compression and torsion was also conducted. Normalized buckling interaction curves that include curves for a geometrically perfect shell, a shell with the actual measured imperfection, a shell with a $\mu_w + \sigma_w$ imperfection, a shell with a $\mu_w - \sigma_w$ imperfection, a shell with a linear-bifurcation-mode imperfection, and the corresponding NASA SP-8007 design curves are shown for shells C1–C3 in Figs. 10–12, respectively. The measured experimental buckling load for the compression loading is indicated in Figs. 10–12 by the solid circular symbol and is included for comparison. The critical compression and torsion loads, P and T, are predicted from a geometrically nonlinear analysis and are normalized with respect to the corresponding the linear bifurcation buckling loads P_{bif} and T^{+}_{bif} of a geometrically perfect shell. The superscript + indicates results for a positive torsion load. A summary of linear bifurcation buckling loads for shells C1–C3 is presented in Table 2.

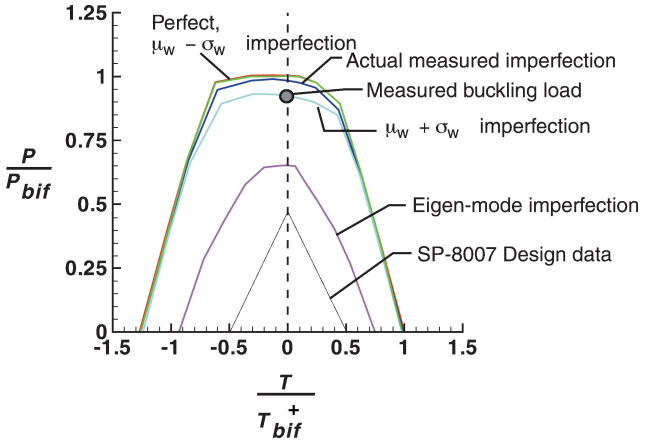

Fig. 10 Predicted buckling interaction curves for axially stiff orthotropic shell C1 subjected to combined axial compression and torsion.

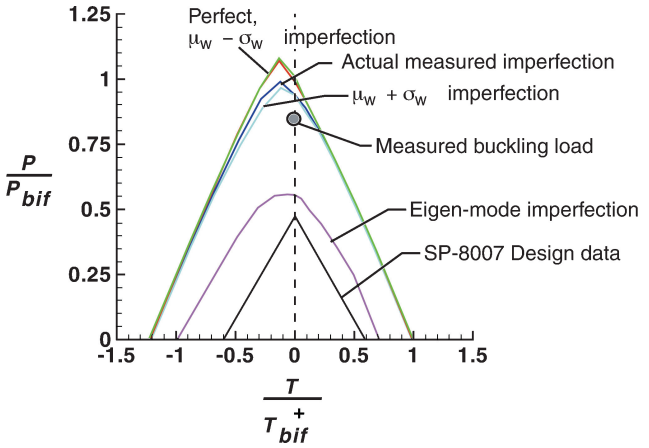

Fig. 11 Predicted buckling interaction curves for circumferentially stiff orthotropic shell C2 subjected to combined axial compression and torsion.

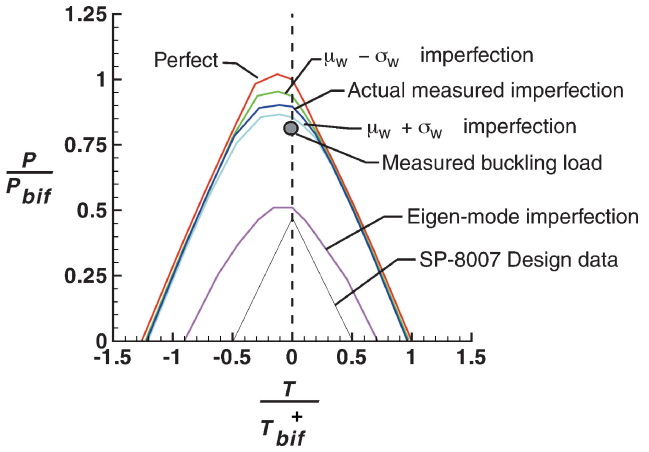

Fig. 12 Predicted buckling interaction curves for quasi-isotropic shell C3 subjected to combined axial compression and torsion.

The predicted results shown in Figs. 10–12 indicate that the buckling interaction curves for the geometrically perfect and imperfect shells are skewed with respect to the plane given by $T = 0$. The skewing is caused by the fact that the diagonal compression caused by the shear load is aligned with the outer 45-deg fibers for the case of negative shear and is perpendicular to the fibers for the case of positive shear. Thus, for a negative-shear load, the shell is stiffer. In addition, the buckling interaction curves are concave and are highly dependent on the laminate stacking sequence. This behavior is similar to the buckling behavior of anisotropic plates that are subjected to combined compression and shear loads presented in Refs. 37 and 38. In contrast, the NASA SP-8007 design guideline assumes a linear relationship between the critical compression-buckling load and the torsion-buckling load. Moreover, the bilinear curve is symmetric about $T = 0$ because the results in NASA SP-8007 are for isotropic shells.

The results in Figs. 10–12 show that shells C1–C3 are sensitive to the as-measured imperfections and the $\mu_w + \sigma_w$ imperfection when the shell is subjected to compression-dominated loading. However, as the torsion load increases, the predicted buckling loads exhibit significantly less imperfection sensitivity for these particular imperfection shapes. The regions of the buckling load interaction curves for which the imperfection sensitivity exists is strongly dependent on the laminate stacking sequence. For example, the buckling-load interaction curves for shell C1 exhibit a relatively large region of imperfection sensitivity for normalized torsion loads T/T^{+}_{bif} that ranges from -0.9 to 0.5 and normalized compression loads P/P_{bif} that range from 0.65 to 0.97, as shown in Fig. 10. However, the regions of imperfection sensitivity in shells C2 and C3 are significantly smaller than that exhibited by shell C1, as shown in Figs. 11 and 12, respectively. In contrast, the results indicate that a shell with a linear-bifurcation-mode imperfection exhibits a significant reduction in the buckling loads for all load cases. The large difference in the response trends is caused by a fundamental difference in the shape of the imperfections in the shell and how they couple with the initial buckling-deformation response of the shell. Specifically, the linear-bifurcation-mode imperfection is similar in character to the initial buckling response in the shell and, thus, exhibits a very strong coupling with the initial buckling deformation of the shell. In contrast, the actual measured imperfection and the imperfection signature, with imperfection amplitudes as large as $w_0/t = 1.92$, are primarily a long-wave imperfection, and these imperfection shapes do not exhibit an artificial strong coupling with the buckling deformations in this shell; thus, the reduction in the buckling load imperfection sensitivity is much less pronounced. In general, the results for shells with linear-bifurcation-mode imperfections are, for the relatively small value of the imperfection amplitude considered here, ultraconservative. Similarly, the lower-bound design recommendation obtained by using NASA SP-8007 for the corresponding isotropic shell is also ultraconservative, as expected, and misrepresents the behavioral trends.

Finally, note that, although no test data were obtained for a C3-type shell subjected to torsion or combined torsion and compression, it is expected that the results for the shell with the actual measured imperfection will be very accurate. This expectation is based on the fact that torsion-loaded shells are not compression dominated like the corresponding compression-loaded shells and, as a result, will not exhibit as high of a degree of imperfection sensitivity.

Design Implications

The approach presented herein for developing shell-buckling design criteria appears to offer a means for obtaining preliminary-design estimates of buckling loads for laminated-composite cylindrical shells subjected to combined loads, without having to resort to extensive testing programs. In addition, this approach offers a relatively affordable alternative to relying on historical test data for shells that do not represent the configuration, material system, or fabrication process associated with the design of interest. This design-criteria-development approach could be used as a tool in the early stages of a design process to determine refined estimates of the buckling loads for the actual as-built shell structure under consideration. To ensure success for problems of interest where refined design criteria are nonexistent, this approach should always be used with a selected number of carefully conducted tests that should be used to validate the finite element analyses and provide confidence in the design results. The validation tests should be carefully conducted so that representative analysis results can be generated to correlate with test results. The provenience and pedigree of each test specimen should be determined or measured to assure that the appropriate shell-wall geometry and thickness distribution, material

properties, and fabrication process-specific effects are included in the analysis used to develop the design criteria.

The design-criteria-development approach described herein has wider implications, that is, it can be used to generate buckling design curves for commonly used structural forms and material systems that account for manufacturing-process imperfections and provide reliable estimates of buckling resistance that are suitable for preliminary design. Design curves of this fidelity will essentially provide a scientifically based replacement for the overly conservative empirical knockdown factors typically used in design today to account for imperfection sensitivity of shell structures. Once a database of manufacturing-process-specific imperfections is established by the technical community, designers will be able to determine which various imperfections are representative of the manufacturing procedure or fabrication process that is appropriate for their designs and then use the relevant design curves. This approach will enable industry to develop a given design without having to repeatedly pay for extensive development tests to develop design knockdown factors. In addition, the refined design criteria should yield substantial weight savings in a given design.

Summary

A new analysis-based approach for developing shell-buckling design criteria for laminated-composite cylindrical shells made of graphite–epoxy material with a tape-laying process has been presented. This approach accounts for the effects of the actual measured initial geometric imperfections in a manner that is suitable for the development of preliminary design data for this class of shells. In particular, a characteristic manufacturing imperfection signature has been identified from the actual measured geometric imperfections for six laminated graphite–epoxy shells and the process used to synthesize the imperfection signature has been discussed in detail. More specifically, a first-approximation mean imperfection shape and the corresponding standard deviation of the imperfection shape were determined from the measured imperfection data for the six shells. Then, a first-approximation imperfection signature was used with high-fidelity nonlinear finite element analyses to predict the buckling behavior of the three shells for uniaxial compression loading, torsion loading, and for combined uniaxial compression and torsion loading. Detailed comparisons of the analytical buckling predictions obtained by using the first-approximation imperfection signature, by using the actual measured imperfection data, and by using a linear-bifurcation-mode imperfection shape, and with test results have been presented. Moreover, comparisons with the corresponding results obtained by extrapolating the lower-bound design data given in NASA SP 8007 to the laminated-composite shells have been presented. In addition, the high-fidelity nonlinear shell analysis procedure used to predict the buckling and nonlinear response of the shells has been described and response characteristics have been discussed.

The results presented herein indicate that the predicted buckling loads for the shells obtained by using the actual measured imperfection shapes in the finite element analyses agree well the corresponding experimentally measured buckling loads for the compression-loaded shells, for example, 10% maximum difference between predicted buckling loads with actual measured imperfection and the corresponding measured buckling loads. With regard to the first-approximation imperfection signature, the results show that, for the most part, the predicted buckling interaction curves for combined compression-torsion loadings that were obtained by using the actual measured imperfection shape fall within the corresponding interaction curves for plus or minus one standard deviation. In addition, comparisons of the nonlinear finite element analyses show that the first-approximation imperfection signature yields response characteristics that are similar to those obtained by using the actual measured imperfection data in the analyses. These results are significant because one-standard-deviation bounds to the test data and the reproduction of significant nonlinear behavioral characteristics represent necessary conditions that should be met by a first-approximation imperfection signature that is to be used to develop an analysis-based design criteria. In contrast, the results also show that buckling interaction curves obtained analytically by using a linear-bifurcation-mode imperfection shape and the curves obtained by using the lower-bound experimental data in NASA SP 8007 are ultraconservative. Overall, the results indicate that the analysis-based approach for developing reliable preliminary-design criteria that has been presented herein has the potential to provide improved, less conservative buckling-load estimates and to reduce the weight and cost of developing buckling-resistant shell structures.

References

[1]Bushnell, D., *Computerized Buckling Analysis of Shells*, Kluwer Academic, Boston, 1989; also U.S. Air Force Wright Aeronautical Lab., AFWAL-TR-81-3049, Wright–Patterson AFB, OH, Dec. 1981.

[2]Singer, J., Árbocz, J., and Weller, T., *Buckling Experiments: Experimental Methods in Buckling of Thin-Walled Structures*, Vol. 2, Wiley, New York, 2002.

[3]von Kármán, T., and Tsien, H. S., "The Buckling of Thin Cylindrical Shells Under Axial Compression," *Journal of the Aeronautical Science*, Vol. 8, No. 8, 1941, pp. 303–312.

[4]Donnell, L. H., and Wan, C. C., "Effect of Imperfections on Buckling of Thin Cylinders and Columns Under Axial Compression," *Journal of Applied Mechanics*, Vol. 17, No. 1, 1950, pp. 73–83.

[5]Koiter, W. T., *On the Stability of Elastic Equilibrium*, H. J. Paris, Amsterdam, 1945 (in Dutch); translation U.S. Air Force Flight Dynamics Lab., AFFDL-TR-70-25, Wright–Patterson AFB, OH, Feb. 1970.

[6]"Buckling of Thin-Walled Circular Cylinders," NASA Space Vehicle Design Criteria, NASA SP-8007, Sept. 1965, rev. 1968.

[7]"Buckling of Thin-Walled Truncated Cones," NASA Space Vehicle Design Criteria, NASA SP-8019, Sept. 1968.

[8]"Buckling of Thin-Walled Doubly Curved Shells," NASA Space Vehicle Design Criteria, NASA SP-8032, Aug. 1969.

[9]Budiansky, B., "Theory of Buckling and Postbuckling Behavior of Elastic Structures," *Advances in Applied Mechanics*, Vol. 14, 1974, pp. 1–65.

[10]Árbocz, J., and Hol, J. M. A. M., "ANILISA—Computational Module for Koiter's Imperfection Sensitivity Theory," Faculty of Aerospace Engineering, Delft Univ. of Technology, Rept. LR-582, Delft, The Netherlands, Jan. 1989.

[11]Khot, N. S., and Venkayya, V. B., "Effect of Fiber Orientation on Initial Postbuckling Behavior and Imperfection Sensitivity of Composite Cylindrical Shells," U.S. Air Force Flight Dynamics Lab., AFFDL-TR-70-125, Wright–Patterson AFB, OH, Dec. 1970.

[12]Cohen, G. A., and Haftka, R. T., "Sensitivity of Buckling Loads of Anisotropic Shells of Revolution to Geometric Imperfections and Design Changes," *Computers and Structures*, Vol. 31, No. 6, 1989, pp. 985–995.

[13]Tennyson, R. C., "Buckling of Laminated Composite Cylinders: A Review," *Composites*, Vol. 6, No. 1, 1975, pp. 17–24.

[14]Árbocz, J., and Babcock, C. D., Jr., "The Effects of General Imperfections on the Buckling of Cylindrical Shells," *Journal of Applied Mechanics*, Vol. 36, No. 1, 1969, pp. 28–38.

[15]Árbocz, J., and Williams, J. G., "Imperfection Surveys on a 10-ft-Diameter Shell Structure," *AIAA Journal*, Vol. 15, No. 7, 1977, pp. 949–956.

[16]Árbocz, J., and Babcock, C. D., Jr., "Computerized Stability Analysis Using Measured Geometric Imperfections," *Proceedings of the 12th Congress of the International Council of the Aeronautical Sciences*, ICAS-80-20.0, Munich, 1980, pp. 688–701.

[17]Árbocz, J., "The Imperfection Data Bank, a Means to Obtain Realistic Buckling Loads," *Buckling of Shells—A State-of-the-Art Colloquium*, edited by E. Ramm, Springer-Verlag, Berlin, 1982, pp. 535–567.

[18]"NASTRAN User's Manual," NASA SP-222(08),Vol. 2, June 1986.

[19]Rankin, C. C., Brogan, F. A., Loden, W. A., and Cabiness, H. D., "STAGS Users Manual, Version 4.0," Advanced Technology Center, Rept. LMSC P032594, Lockheed Martin Missiles and Space Co., Inc., Palo Alto, CA, May 2001.

[20]Starnes, J. H., Jr., Hilburger, M. W., and Nemeth, M. P., "The Effects of Initial Imperfections on the Buckling of Composite Cylindrical Shells," *Composite Structures—Theory and Practice*, edited by P. Grant and C. Q. Rousseau, ASTM STP 1383, American Society for Testing and Materials, West Conshohocken, PA, 2000, pp. 529–550.

[21]Hilburger, M. H., and Starnes, J. H., Jr., "High-Fidelity Analysis of Compression-Loaded Composite Shells," AIAA Paper 2001-1394, 2001.

[22]Hilburger, M. W., and Starnes, J. H., Jr., "Effects of Imperfections on the Buckling Response of Compression-Loaded Composite Shells," *International Journal of Non-Linear Mechanics*, Vol. 37, No. 4, 2002, pp. 623–643.

[23]Nemeth, M. P., Britt, V. O., Young, R. D., Collins, T. J., and Starnes, J. H., Jr., "Nonlinear Behavior of Space Shuttle Superlightweight Liquid-Oxygen Tank Under Prelaunch Loads," *Journal of Spacecraft and Rockets*, Vol. 36, No. 6, 1999, pp. 788–803.

[24]Nemeth, M. P., Young, R. D., Collins, T. J., and Starnes, J. H., Jr., "Nonlinear Behavior of Space Shuttle Superlightweight Liquid-Oxygen Tank Under End-of-Flight Loads," *Journal of Spacecraft and Rockets*, Vol. 36, No. 6, 1999, pp. 828–835.

[25]Young, R. D., Nemeth, M. P., Collins, T. J., and Starnes, J. H., Jr., "Nonlinear Behavior of Space Shuttle Superlightweight Liquid-Oxygen Tank Under Booster Ascent Loads," *Journal of Spacecraft and Rockets*, Vol. 36, No. 6, 1999, pp. 820–827.

[26]Nemeth, M. P., Young, R. D., Collins, T. J., and Starnes, J. H., Jr., "Effects of Welding-Induced Imperfections on Behavior of Space Shuttle Superlightweight Liquid-Oxygen Tank," *Journal of Spacecraft and Rockets*, Vol. 36, No. 6, 1999, pp. 812–819.

[27]Nemeth, M. P., Young, R. D., Collins, T. J., and Starnes, J. H., Jr., "Effects of Initial Geometric Imperfections on the Nonlinear Response of the Space Shuttle Superlightweight Liquid-Oxygen Tank," *International Journal of Non-Linear Mechanics*, Vol. 37, No. 4-5, 2002, pp. 723–744.

[28]Nemeth, M. P., and Starnes, J. H., Jr., "The NASA Monographs on Shell Stability Design Recommendations–A Review and Suggested Improvements," NASA TP-1998-206290, Jan. 1998.

[29]Árbocz, J., and Starnes, J. H., Jr., "Future Directions and Challenges in Shell Stability Analysis," *Thin-Walled Structures*, Vol. 40, No. 9, 2002, pp. 729–754.

[30]Chryssanthopoulos, M. K., Giavotto, V., and Poggi, C., "Statistical Imperfection Models for Buckling Analysis of Composite Shells," *Buckling of Shell Structures, on Land, in the Sea and in the Air*, edited by J. F. Jullien, Elsevier Applied Science, New York, 1991, pp. 43–52.

[31]Claus, S. J., "Manufacture–Structure–Performance Relationships for Filament-Wound Composite Shells," Ph.D. Dissertation, Engineering Science and Mechanics Dept., Pennsylvania State Univ., University Park, PA, May 1994.

[32]Árbocz, J., and Elishakoff, I., "Reliability of Axially Compressed Cylindrical Shells with General Nonsymmetric Imperfections," *Journal of Applied Mechanics*, Vol. 107, March 1985, pp. 122–128.

[33]Árbocz, J., Starnes, J. H., Jr., and Nemeth, M.P., "On the Accuracy of Probablistic Buckling Load Predictions," AIAA Paper 2000-1236, 2000.

[34]Riks, E., "Progress in Collapse Analyses," *Journal of Pressure Vessel Technology*, Vol. 109, Feb. 1987, pp. 27–41.

[35]Park, K. C., "An Improved Stiffly Stable Method for Direct Integration of Nonlinear Structural Dynamics," *Journal of Applied Mechanics*, Vol. 42, June 1975, pp. 464–470.

[36]Bushnell, D., "Static Collapse: A Survey of Methods and Modes of Behavior," *Collapse Analysis of Structures*, PVP-Vol. 84, American Society of Mechanical Engineers, 1984, pp. 30–32.

[37]Nemeth, M. P., "Buckling Behavior of Long Symmetrically Laminated Plates Subjected to Combined Loadings," NASA TP-3195, May 1992.

[38]Nemeth, M. P., "Buckling Behavior of Long Anisotropic Plates Subjected to Combined Loads," NASA TP-3568, Nov. 1995.

K. Shivakumar
Associate Editor